J. Mech. Phys. Solids 171 (2023) 105123

Contents lists available at ScienceDirect

Journal of the Mechanics and Physics of Solids

journal homepage: www.elsevier.com/locate/jmps

A mixed mode phase-field model of ductile fracture

William Huber, Mohsen Asle Zaeem *

Department of Mechanical Engineering, Colorado School of Mines, CO 80401, USA

ARTICLE INFO

Keywords:
Ductile fracture
Phase-field model
Mixed Mode

ABSTRACT

We present the first mixed mode phase-field model of ductile fracture. The contribution of crack opening and shearing deformations to the propagation of a crack is expressed by introducing two phase fields. Constitutive relations are then introduced to couple and distinguish these phase fields. Special attention is given to the maximum shear stress and its effect on the development of fractures. The proposed model is validated by tensile testing experiments found in the literature on Al 2024 T-351. Model predictions of the crack path and load-displacement response are compared to a plane-strain tension experiment, a round bar tension experiment and a notched round bar tension experiment. The model is shown to accurately capture the slant and cup-cone crack paths as well as force-displacement curves.

1. Introduction

The fracture of ductile materials is a complex, multiscale process which results in the loss of load bearing capacity and can be catastrophic for engineering structures. In contrast to brittle fractures, for which Griffith's criterion (Griffith, 1921) applies well, ductile fracture features a large inelastic process zone due to the severe plastic deformation ahead of a crack tip.

To predict fracture in ductile materials, some of the computational approaches that have been proposed and implemented into finite element codes are the cohesive zone models, continuum damage models, and element deletion techniques. The cohesive zone model (De Borst, 2003; de Borst et al., 2006; Scheider and Brocks, 2006) is a discrete fracture approach where the numerical representation of the fracture surface features two distinct crack faces. Since the cohesive zone model requires that cohesive elements are placed on element edges, the prediction of deflected crack paths is heavily dependent on the mesh. On the other hand, the continuum damage approach (Chaboche, 1988; Krajcinovic and Lemaitre, 1987; Lemaitre, 1985; Needleman and Tvergaard, 1994; Peerlings et al., 1998) seeks to represent a continuous concentration of flaws which, in turn, affect the yield strength and elastic properties of the material. Continuum damage models and element deletion techniques are frequently used in conjunction with each other where a finite element (or its stiffness) are removed upon the fulfillment of a fracture criteria. Both of these methods introduce a severe mesh dependence on the mechanical response of material. Within this class of models, there are micromechanical and phenomenological approaches. Micromechanical models such as the models of Gurson (1977) and Tvergaard (1981) are based on the homogenization of a representative volume element containing voids to describe the evolution of damage at the macroscale. Phenomenological approaches such as the GISSMO (Andrade et al., 2016) model and the models of Rousselier (1987), Lemaitre (1985), Johnson and Cook (1985), and Xue and Wierzbicki (2008) are based on empirical relations around stress states and plastic deformation to describe the onset and propagation of damage. These approaches are popular as they are able to easily incorporate the effects of the I_1, J_2, and J_3 stress invariants.

* Corresponding author.
E-mail address: zaeem@mines.edu (M. Asle Zaeem).

https://doi.org/10.1016/j.jmps.2022.105123
Received 1 July 2022; Received in revised form 22 September 2022; Accepted 25 October 2022
Available online 30 October 2022

The phase-field method is able to overcome many of the shortcomings presented by the aforementioned approaches. In this approach, a phase-field parameter represents cracked states, while the coupling between displacements and the phase field takes the form of a degradation of strain energy as a function of the phase-field parameter. The phase-field method for fracture was established by Bourdin et al. (2000) who showed its convergence towards Francfort and Marigo's variational theory for brittle fracture (Francfort and Marigo, 1998) in linear elastic materials. The crack path is determined along with the displacement field by seeking the fracture path as a consequence of maximum dissipation. Additionally, this approach features a well-defined amount of fracture dissipation, which is independent of a sufficiently fine mesh and regularization length (de Borst and Verhoosel, 2016; Wu et al., 2020). The phase-field approach results in a set of coupled mechanical and phase-field constitutive relations, and the solution of the phase-field equilibrium equation in conjunction with mechanical equilibrium yields crack paths and displacements. The phase-field fracture approach has since been used in conjunction with visco-elastic (Yin and Kaliske, 2020b), elasto-plastic (Ambati et al., 2015; Ambati et al., 2016; Borden et al., 2016; Duda et al., 2015; Kuhn et al., 2016; Miehe, et al., 2016,2015), crystal plasticity (De Lorenzis et al., 2016), solid state phase transformation (Schmitt et al., 2015; Simoes and Martínez-Pañeda, 2021) material models and has been extended to anisotropic and heterogenous materials (Lotfolahpour and Asle Zaeem, 2021).

The extension of the phase-field fracture approach to ductile materials is the primary consideration of the present work. In the past, Duda et al. (2015) formulated a small-strain model where the growth of the phase-field was driven by elastic strain energy, and the plastic dissipation was a function of only the plastic strain. More recently, Ambati et al. (2015, 2016) proposed a model for finite strains where the degradation of elastic strain energy was made a function of both the phase-field parameter and the plastic strain. Other approaches have involved the introduction of thresholds for the nucleation of the phase-field. An example of this approach was proposed by Borden et al. (2016), where a threshold for the contribution of plastic dissipation to the evolution of the phase-field and a degradation of the plastic potential reproduces some basic aspects of ductile fracture phenomenology. A similar, non-variational approach was considered by Miehe et al. (2015). Alternatively, another similar approach was taken by Aldakheel et al. (2018), where the void volume fraction computed from the Gurson, Tvergaard and Needleman (GTN) model (Tvergaard, 1981) was used to evolve the phase-field parameter upon reaching a critical void volume fraction. Such an approach makes the fracture initiation and propagation dependent on both the accumulated plastic strain and triaxiality. Furthermore, Yin and Kaliske (2020a) proposed a different interpretation of the ductile fracture process, where plastic strain degrades the fracture toughness. All of the aforementioned approaches lead to situations in which the mechanical and fracture properties of a material become difficult to calibrate, and predictions of crack path are not always reliable. Further, only a few of the previously proposed formulations consider the effect of stress state on the initiation and propagation of fractures in ductile materials in a quantitative manner. To summarize, these approaches lead to difficulties in the simultaneous prediction of the crack path and mechanical response, since there is no distinction made between the shearing and opening characters of the ductile fracture process. For example, Li et al. (2022) incorporated the Modified Mohr-Coulomb criterion (which is dependent on lode angle and stress triaxiality) into a phase field fracture model but was not able to accurately predict crack paths because the proposed stress-degradation scheme favored crack paths normal to the loading axis. On the other hand, Miehe et al. (2016) were able to predict realistic crack paths for tension experiments but did not consider the effect of the lode angle or maximum shear stress on the initiation of a crack which, limits its applicability to plane strain or shear dominated loading scenarios.

Phase-field fracture models which distinguish between tensile and shearing deformations have been proposed for quasi-brittle geomaterials in the field of rock-mechanics. For example, Spetz et al. (2021) proposed a non-variational model with a single order parameter for fracture, in which the tensile and shear contributions to the fracture driving force are weighted by their relative critical energy release rates. On the other hand, Fei and Choo (2021) proposed a model with two order parameters, one for mode I cracks and another for mode II. To the best of our knowledge, such a description of fracture in ductile metals has yet to be attempted. In this work, we propose an alternative formulation to the previous ductile fracture phase field models, in which the mode I surface energy is distinguished from the mode II surface energy, and order parameters are assigned to each mode. Constitutive relations are then chosen to effect a shearing or opening deformation depending on the stress state.

2. Model formulations

2.1. Finite deformations and state variables

For a solid domain Ω with boundary S, $\boldsymbol{X}$ defines the coordinates of the reference configuration and $\boldsymbol{x}$ defines the coordinates of the current configuration. The deformation gradient is defined as $\boldsymbol{F} = \nabla_{\boldsymbol{X}}\boldsymbol{x} = \nabla_{\boldsymbol{X}}\boldsymbol{u} + \boldsymbol{I}$, where $\boldsymbol{u}$ represents the displacement of a material point and $\boldsymbol{I}$ is the second order identity tensor. The deformation gradient is multiplicatively decomposed into elastic and inelastic parts as follows:

$$\boldsymbol{F} = \boldsymbol{F}^{e}\boldsymbol{F}^{ie} \tag{1}$$

where $\boldsymbol{F}^{e}$ is the elastic deformation gradient, and $\boldsymbol{F}^{ie}$ is the inelastic deformation gradient. The inelastic deformation gradient is composed of a "bulk" plastic part and a "sliding" part, similar to the discrete discontinuity formulation presented by Liu and Borja (2009):

$$\boldsymbol{F}^{ie} = \boldsymbol{F}^{p}\boldsymbol{F}^{s} \tag{2}$$

where $\boldsymbol{F}^{p}$ is the bulk plastic deformation gradient, and $\boldsymbol{F}^{s}$ is the sliding deformation gradient. The bulk plastic deformation represents

diffuse inelastic deformation, such as that which contributes to strain hardening, while the sliding deformation represents the localized deformation due to shear localization associated with strain softening. This approach is also similar to the approach considered in the viscous model of Shanthraj et al. (2017) where a crack is considered through an inelastic deformation gradient. Furthermore, the Green Lagrange strain is defined as:

$$\boldsymbol{E} = \frac{1}{2}(\boldsymbol{C} - \boldsymbol{I});\ \boldsymbol{C} = \boldsymbol{F}^T\boldsymbol{F}, \tag{3}$$

where $\boldsymbol{C}$ is the Cauchy – Green deformation tensor. To enable the additive decomposition of strain in the formulation of the constitutive relations, the Lagrangian Hencky strain is chosen (de Souza Neto et al., 2011). The Hencky strain is given by:

$$\boldsymbol{\varepsilon} = \frac{1}{2}\ln(\boldsymbol{C}). \tag{4}$$

The elastic strain is then given by:

$$\boldsymbol{\varepsilon}^e = \boldsymbol{\varepsilon} - \boldsymbol{\varepsilon}^{ie} \tag{5}$$

where $\boldsymbol{\varepsilon}^{ie}$ is the inelastic strain which is composed of:

$$\boldsymbol{\varepsilon}^{ie} = \boldsymbol{\varepsilon}^p + \boldsymbol{\varepsilon}^s, \tag{6}$$

where $\boldsymbol{\varepsilon}^p$ is the bulk plastic strain and $\boldsymbol{\varepsilon}^s$ is the sliding strain.

For the representation of the crack mode I and mode II crack phase-field variables, ϕ_I and ϕ_{II} respectively, are introduced to distinguish cracked and un-cracked regions. Cracked regions take a value of 1, while uncracked regions take a value of 0. Additionally, the crack phase-fields are subject to the condition of irreversibility, $\dot{\phi}_I \geq 0$ and $\dot{\phi}_{II} \geq 0$. To summarize, the state variables involved in the determination of the thermodynamic state of the body are these variables: $\boldsymbol{u},\ \boldsymbol{\varepsilon}^p,\ \boldsymbol{\varepsilon}^s,\ \phi_I, \phi_{II}$.

2.2. Energetic formulation

In this work, the total energy functional is composed of elastic, bulk-plastic, sliding, mode I fracture and mode II fracture energies, as follows:

$$\Pi(\boldsymbol{u}, \bar{\varepsilon}^p, \bar{\varepsilon}^s, \phi_I, \phi_{II}) = \int_\Omega \left[\psi^e(\boldsymbol{u}, \bar{\varepsilon}^p, \bar{\varepsilon}^s, \phi_I) + \psi^p(\bar{\varepsilon}^p) + \psi^s(\bar{\varepsilon}^s, \phi_{II}) + \psi_I^f(\phi_I) + \psi_{II}^f(\phi_{II})\right] d\Omega - \int_S \boldsymbol{t}\cdot\boldsymbol{u}\, dS \tag{7}$$

where, ψ^e is the elastic strain energy density, $\bar{\varepsilon}^p$ and $\bar{\varepsilon}^s$ are respectively the equivalent bulk plastic and sliding strains, ψ^p is the plastic energy density, ψ^s is the sliding energy density, ψ_I^f is the mode I fracture energy, ψ_{II}^f is the mode II fracture energy, and $\boldsymbol{t}$ is traction.

2.3. Elastic strain energy density

The elastic strain energy density function is given by:

$$\psi^e = \bar{\psi}^e\ + (g_I(\phi_I) - 1)\bar{\psi}_I^e, \tag{8}$$

where $g_I(\phi_I)$ is the mode I degradation function. The degradation function effects a loss of stiffness where the mode I crack phase-field develops. In this work, the following degradation function is adopted from Lorentz and Godard (2011), since it allows for the definition of a damage free threshold:

$$g_I(\phi_I) = \frac{(1-\phi_I)^2}{(1-\phi_I)^2 + m_I\phi_I(1+\phi_I)};\ m_I = \frac{3G_{cI}}{4L_I\psi_{cI}}, \tag{9}$$

where G_{cI} is the mode I critical energy release rate, L_I is the regularization length scale and ψ_{cI} is the energetic damage threshold. On the other hand, $\bar{\psi}^e$ is called the undamaged elastic strain energy and is given by:

$$\bar{\psi}^e = \frac{1}{2}\boldsymbol{\varepsilon}^e : \boldsymbol{C} : \boldsymbol{\varepsilon}^e \tag{10}$$

where $\boldsymbol{C}$ is the isotropic elastic tensor. $\bar{\psi}_I^e$ defines the portion of the elastic strain energy which drives mode I fracture and is given by :

$$\bar{\psi}_I^e = \frac{1}{2}\left(\frac{<\bar{\sigma}_1>_+^2}{2(\lambda+2\mu)}\right), \tag{11}$$

where $\bar{\sigma}_1$ is the undamaged first principal stress and $< x >_+$ is an operator which returns a 0 when the argument is negative and the argument if it is positive. λ and μ are Lame's elastic constants. The Cauchy stress is given by:

$$\boldsymbol{\sigma} = \frac{\partial \psi^e}{\partial \boldsymbol{\varepsilon}^e}, \tag{12}$$

The 2nd Piola Kirchoff stress is given by:

$$\boldsymbol{S} = \boldsymbol{F}^T \boldsymbol{\sigma} \boldsymbol{F}. \tag{13}$$

2.4. Bulk plastic and sliding energy density

The plastic energy density function is given by:

$$\psi^p = \int_0^{\bar{\varepsilon}^p} \sigma_y(\bar{\varepsilon}^p) d\bar{\varepsilon}^p, \tag{14}$$

where σ_y is the yield stress which is dependent on $\bar{\varepsilon}^p$ due to hardening. Meanwhile, the sliding energy density function is given by:

$$\psi^s = g(\phi_{II}) \tau_f \bar{\varepsilon}^s, \tag{15}$$

where $g(\phi_{II})$ is the mode II degradation function which is given by:

$$g(\phi_{II}) = (1 - \phi_{II})^2. \tag{16}$$

And τ_f is the critical mode II failure stress.

2.5. Fracture energy

The chosen form of the mode I fracture energy is frequently referred to as the AT1 functional (Wu et al., 2020), which allows the definition of a threshold (ψ_{cI}) for the nucleation of the phase-field when used in tandem with the degradation function adopted from Lorentz and Godard (2011). The mode I fracture energy is defined as:

$$\psi_I^f = G_{cI} \frac{3}{4 L_I} \left(\phi_I + \frac{L_I^2}{4} |\nabla \phi_I|^2 \right), \tag{17}$$

where G_{cII} is the mode II critical energy release rate, and L_{II} is the regularization length scale with the pre-factors adopted from Geelen et al. (2019). On the other hand, for mode II, a damage threshold is automatically present, since $\tau_f \bar{\varepsilon}^s$ can only be greater than 0 when the equivalent stress for sliding is greater than τ_f. Therefore, the so called AT2 functional (Wu et al., 2020) will be chosen for defining the mode II fracture energy:

$$\psi_{II}^f = G_{cII} \frac{1}{2 L_{II}} \left(\phi_{II}^2 + L_{II}^2 |\nabla \phi_{II}|^2 \right), \tag{18}$$

where G_{cII} is the mode II critical energy release rate, and L_{II} is the regularization length scale with the pre-factors adopted from Miehe et al. (2015). A different regularization length scale parameter is associated with mode II (L_{II}) and mode I (L_I). This is because the AT1 functional yields a different phase field topology than the AT2 functional. Therefore, L_I and L_{II} should be chosen so that the localization widths of ϕ_I and ϕ_{II} are similar. In the 2D examples provided in this work, $L_{II} = \frac{1}{4} L_I$.

To summarize, two different fracture energies are adopted for mode I and mode II (AT1 and AT2 respectively). This is a consequence of reproducing a "brittle" elastic softening behavior for mode I, while for mode II, inelastic softening is considered. For both modes a nucleation criterion for the phase field is defined, albeit in different ways. The use of the mode I degradation function in Eq. (9), along with the mode I fracture energy in Eq. (17), defines a threshold for the nucleation of ϕ_I as explained in Geelen et al. (2019). However, the use of the mode II degradation function in Eq. (16) and the mode II fracture energy in Eq. (18) do not naturally produce a threshold. Instead, a threshold for the nucleation of $\bar{\varepsilon}^s$ is defined in the next section. This, in turn, defines a threshold for the nucleation of ϕ_{II} because if $\tau_f \bar{\varepsilon}^s = 0$, then ϕ_{II} must also be 0.

2.6. Evolution of state variables

Application of the stationary condition to Eq. (7) in the material configuration yields:

$$\delta\Pi = \int_{\Omega} \boldsymbol{S} : \delta\boldsymbol{E}(\boldsymbol{u})d\Omega + \int_{\Omega} \left(F_{BP}(\boldsymbol{\sigma}) - \sigma_y(\bar{\varepsilon}^p)\right)\delta\bar{\varepsilon}^p d\Omega + \int_{\Omega} \left(F_S(\boldsymbol{\sigma}) - g(\phi_{II})\tau_f\right)\delta\bar{\varepsilon}^s +$$
$$\int_{\Omega} \left(\left(g^{'}(\phi_I)\bar{\psi}^e + \frac{3G_{cI}}{4L_I}\right)\delta\phi_I + \frac{3}{8}G_{cI}L_I\nabla\phi_I \cdot \nabla\delta\phi_I \right) d\Omega + \int_{\Omega} \left(\left(g^{'}(\phi_{II})\tau_f\bar{\varepsilon}^s + \frac{G_{cII}}{L_I}\phi_{II}\right)\delta\phi_{II} + G_{cII}L_{II}\nabla\phi_{II} \cdot \nabla\delta\phi_{II} \right) d\Omega \tag{19}$$
$$-\int_S \boldsymbol{t} \cdot \delta\boldsymbol{u} dS \geq 0$$

where the δ operator indicates a functional derivative. This leads to the strong form:

$$\nabla_X \cdot (\boldsymbol{FS}) = 0 \tag{20}$$

$$F_{BP}(\boldsymbol{\sigma}) - \sigma_y(\bar{\varepsilon}^p) \leq 0, \tag{21}$$

$$F_S(\boldsymbol{\sigma}) - g(\phi_{II})\tau_f \leq 0, \tag{22}$$

$$\frac{3G_{cI}}{4L_I}\left(\frac{L_I^2}{2}\Delta\phi_I - 1\right) - g^{'}(\phi_I)\psi_I^e = 0, \tag{23}$$

$$\frac{G_{cII}}{L_{II}}\left(L_{II}^2\Delta\phi_{II} - \phi_{II}\right) - g^{'}(\phi_{II})\tau_f\bar{\varepsilon}^s = 0. \tag{24}$$

$F_{BP}(\boldsymbol{\sigma})$ and $F_S(\boldsymbol{\sigma})$ are the equivalent stresses for the bulk plasticity yield surface and the slipping yield surface, respectively. The equivalent stress for bulk plasticity is the von Mises stress which is defined as:

$$F_{BP}(\boldsymbol{\sigma}) = \sigma_{vm} = \sqrt{3J_2(\boldsymbol{\sigma})}. \tag{25}$$

The evolution of $\boldsymbol{\varepsilon}^p$ is defined as:

$$d\boldsymbol{\varepsilon}^p = d\lambda_{BP}\frac{\partial F_{BP}}{\partial\boldsymbol{\sigma}}, \tag{26}$$

where λ_{BP} is a Lagrange multiplier, which is evaluated numerically by the fully implicit return mapping procedure provided in de Souza Neto et al. (2011). On the other hand, the equivalent stress for mode II sliding is given by a pressure modified maximum shear stress (τ_{max}) criterion (Drucker, 1953; Xue, 2009):

$$F_S(\boldsymbol{\sigma}) = (\sigma_1 - \sigma_3) + \alpha p, \tag{27}$$

where σ_1 and σ_3 are the first and third principal stresses, respectively. α is a material parameter to effect pressure dependence on the yield surface, where pressure is defined by $p = \frac{I_1(\boldsymbol{\sigma})}{3}$. This yield function was chosen because shear bands propagate on planes of maximum shear and are sensitive to the shear stress on those planes (Donovan, 1988; Lee and Ghosh, 1996; Lloyd, 2003; Yang et al., 2011). The evolution of $\boldsymbol{\varepsilon}^s$ is then given by:

$$d\boldsymbol{\varepsilon}^s = d\lambda_s\frac{\partial F_s}{\partial\boldsymbol{\sigma}}, \tag{28}$$

where λ_S is a Lagrange multiplier. The Lagrange multiplier λ_S is solved for numerically using the fully implicit return mapping procedure found in de Souza Neto et al. (2011).

2.7. Mode I – Mode II coupling

In order to allow the nucleation of a tensile crack within a developing shearing instability, another degradation function is introduced to degrade the mode I fracture properties. Specifically, the energetic damage threshold, ψ_{cI}, and the mode I critical energy release rate, G_{cI}, are multiplied by the following degradation function:

$$f(\phi_{II}) = (1 - \phi_{II})^2 + c, \tag{29}$$

where c is a material parameter which ranges from [0,1] and defines a lower limit for the degradation of mode I fracture properties. Although a physical interpretation of the value of c is difficult to determine, it should be chosen to be greater than 0 and significantly less than 1. ψ_{cI} and G_{cI} must accordingly be modified so that:

$$\psi_{cI} = f(\phi_{II})\left(\psi_{cI}^* - c\psi_{cI}^*\right) + c^2\psi_{CI}^*, \tag{30}$$

$$G_{cI} = f(\phi_{II})\left(G_{cI}^* - cG_{cI}^*\right) + c^2G_{cI}^*, \tag{31}$$

where ψ_{cI}^{*} and G_{cI}^{*} are the initial values of ψ_{cI} and G_{cI}. The degradation is only introduced for mode I fracture properties since there is no shear stress on planes of maximum principal stress. Similar to the fracture mode coupling schemes in cohesive zone models (Scheider and Brocks, 2003), the introduced coupling between ϕ_{II} and ϕ_{I} does not have an obvious physical basis. Instead, the coupling is introduced to yield realistic kinematics of the crack nucleation and propagation process.

2.8. Solution scheme and implementation

The following weak form equations are discretized and solved by finite elements through the Mathematics Module of the COMSOL Multiphysics software (COMSOL, 2018).

$$\int_{\Omega} \boldsymbol{S} : \delta \boldsymbol{E}(\boldsymbol{u}) d\Omega - \int_{S} \boldsymbol{t} \cdot \delta \boldsymbol{u} dS = 0 \tag{32}$$

$$\int_{\Omega} \left(\left(g^{'}(\phi_I) H_I + \frac{3G_{cI}}{4L_I} \right) \delta\phi_I + \frac{3}{8} G_{cI} L_I \nabla\phi_I \cdot \nabla\delta\phi_I \right) d\Omega = 0, \tag{33}$$

$$\int_{\Omega} \left(\left(g^{'}(\phi_{II}) \tau_f \bar{\varepsilon}^{s} + \frac{G_{cII}}{L_{II}} \phi_{II} \right) \delta\phi_{II} + G_{cII} L_{II} \nabla\phi_{II} \cdot \nabla\delta\phi_{II} \right) d\Omega = 0. \tag{34}$$

Here H_I is the history field of the fracture driving force (Miehe et al., 2010), which ensures the irreversibility of the mode I crack phase-field ϕ_I. This field is evaluated according to the following equation:

$$H_{n+1} = \max(\bar{\psi}^{e}, H_n), \tag{35}$$

where n denotes the previous solution increment. The mode II phase-field evolution does not require a history field since $\bar{\varepsilon}^{s}$ is inelastic.

The computation of λ_{BP} is achieved through the fully implicit return mapping procedure (de Souza Neto et al., 2011). A trial state is defined as:

$$\boldsymbol{\varepsilon}_{n+1}^{e,\ trial} = \boldsymbol{\varepsilon}_{n}^{e} + \Delta\boldsymbol{\varepsilon}, \tag{36}$$

$$\boldsymbol{\sigma}_{n+1}^{trial} = \frac{\partial \psi^{e}\left(\boldsymbol{\varepsilon}_{n+1}^{e,\ trial}\right)}{\partial \boldsymbol{\varepsilon}_{n+1}^{e,\ trial}}, \tag{37}$$

$$\sigma_{vm,n+1}^{trial} = \sqrt{3J_2(\boldsymbol{\sigma}_{n+1}^{trial})}, \tag{38}$$

$$p_{n+1}^{trial} = \frac{I_1\left(\boldsymbol{\sigma}_{n+1}^{trial}\right)}{3}. \tag{39}$$

When the yield condition is triggered, a return mapping back onto the yield surface is performed by solving the following nonlinear equation for $\Delta\lambda_{BP}$:

$$\sigma_{vm,n+1}^{trial} - 3G\Delta\lambda_{BP} - \sigma_y(\bar{\varepsilon}_{n+1}^{p}) = 0. \tag{40}$$

The stresses and $\bar{\varepsilon}^{p}$ are then updated with $\Delta\lambda_{BP}$:

$$\boldsymbol{\sigma}_{n+1} = \left(1 - \frac{\Delta\lambda_{BP} 3G}{\sigma_{vm,n+1}^{trial}} \right) dev\left(\boldsymbol{\sigma}_{n+1}^{trial}\right) + p_{n+1}^{trial}, \tag{41}$$

$$\bar{\varepsilon}_{n+1}^{p} = \Delta\lambda_{BP} + \bar{\varepsilon}_{n}^{p}. \tag{42}$$

The computation of λ_s is also achieved through the fully implicit return mapping procedure. However, the yield surface of the mode II sliding contains singularities which complicates the return mapping. In this work, a similar principal stress based procedure to the return mapping for the Tresca surface described in de Souza Neto et al. (2011) is used. The trial stress state is given by the stress updated by the bulk plasticity return mapping procedure. The principal values of the trial stress are: $\sigma_{1,n+1}^{trial}$, $\sigma_{2,n+1}^{trial}$ and $\sigma_{3,n+1}^{trial}$, with corresponding eigenvectors of $\boldsymbol{e}_1$, $\boldsymbol{e}_2$ and $\boldsymbol{e}_3$, and corresponding deviatoric principal stresses of $s_{1,n+1}^{trial}$, $s_{2,n+1}^{trial}$ and $s_{3,n+1}^{trial}$. When the yield condition is triggered, multiple return mappings may be possible. When the updated stress lies on a plane of the yield surface in principal stress space:

$(s_1 \geq s_2 \geq s_3)$, (43)the following return mapping is valid:

$$s_{1,n+1}^{trial} - s_{3,n+1}^{trial} - 4G\Delta\lambda_s + \alpha\left(p_{n+1}^{trial} - K\alpha\Delta\lambda_s\right) - g_{II}(\phi_{II})\tau_f = 0. \tag{44}$$

With the closed form solution of:

$$\Delta\lambda_s = \frac{s^{trial}_{1,n+1} - s^{trial}_{3,n+1} + \alpha p^{trial}_{n+1} - g_{II}(\phi_{II})\tau_f}{4G - K\alpha^2}. \tag{45}$$

And the corresponding updates are given by:

$$s_{1,n+1} = s^{trial}_{1,n+1} - 2G\Delta\lambda_s, \tag{46}$$

$$s_{2,n+1} = s^{trial}_{2,n+1}, \tag{47}$$

$$s_{3,n+1} = s^{trial}_{3,n+1} + 2G\Delta\lambda_s, \tag{48}$$

$$p_{n+1} = p^{trial}_{n+1} - \alpha K\Delta\lambda_s, \tag{49}$$

$$\bar{\varepsilon}^s_{n+1} = \Delta\lambda_s + \bar{\varepsilon}^s_n. \tag{50}$$

On the other hand, when the updated stress is on a line and

$$s_1 + s_3 - 2s_2 > 0,$$

the following return mapping is valid:

$$s^{trial}_{1,n+1} - s^{trial}_{3,n+1} - 2G\left(2\Delta\lambda^a_s + \Delta\lambda^b_s\right) + \alpha\left(p^{trial}_{n+1} - K\alpha\left(\Delta\lambda^a_s + \Delta\lambda^b_s\right)\right) - g_{II}(\phi_{II})\tau_f = 0, \tag{51}$$

$$s^{trial}_{1,n+1} - s^{trial}_{2,n+1} - 2G\left(\Delta\lambda^a_s + 2\Delta\lambda^b_s\right) + \alpha\left(p^{trial}_{n+1} - K\alpha\left(\Delta\lambda^a_s + \Delta\lambda^b_s\right)\right) - g_{II}(\phi_{II})\tau_f = 0. \tag{52}$$

With this closed form solution of:

$$\Delta\lambda^a_s = \frac{2G\left(s^{trial}_{1,n+1} + s^{trial}_{2,n+1} - 2s^{trial}_{3,n+1} + \alpha p^{trial}_{n+1} - g_{II}(\phi_{II})\tau_f\right) + \alpha^2 K\left(s^{trial}_{3,n+1} - s^{trial}_{2,n+1}\right)}{4G(K\alpha^2 + 3G)}, \tag{53}$$

$$\Delta\lambda^b_s = \frac{2G\left(s^{trial}_{1,n+1} - 2s^{trial}_{2,n+1} + s^{trial}_{3,n+1} + \alpha p^{trial}_{n+1} - g_{II}(\phi_{II})\tau_f\right) + \alpha^2 K\left(s^{trial}_{3,n+1} - s^{trial}_{2,n+1}\right)}{4G(K\alpha^2 + 3G)}, \tag{54}$$

$$\Delta\lambda_s = \Delta\lambda^a_s + \Delta\lambda^b_s. \tag{55}$$

And the corresponding updates are:

$$s_{1,n+1} = s^{trial}_{1,n+1} - 2G\left(\Delta\lambda^a_s + \Delta\lambda^b_s\right), \tag{56}$$

$$s_{2,n+1} = s^{trial}_{2,n+1} + 2G\Delta\lambda^b_s, \tag{57}$$

$$s_{3,n+1} = s^{trial}_{3,n+1} + 2G\Delta\lambda^a_s, \tag{58}$$

$$p_{n+1} = p^{trial}_{n+1} - \alpha K\left(\Delta\lambda^a_s + \Delta\lambda^b_s\right), \tag{59}$$

$$\bar{\varepsilon}^s_{n+1} = \Delta\lambda_s + \bar{\varepsilon}^s_n. \tag{60}$$

Otherwise, when the inequality is violated, the following return mapping is valid:

$$s^{trial}_{1,n+1} - s^{trial}_{3,n+1} - 2G\left(2\Delta\lambda^a_s + \Delta\lambda^b_s\right) + \alpha\left(p^{trial}_{n+1} - K\alpha\left(\Delta\lambda^a_s + \Delta\lambda^b_s\right)\right) - g_{II}(\phi_{II})\tau_f = 0, \tag{61}$$

$$s^{trial}_{2,n+1} - s^{trial}_{3,n+1} - 2G\left(\Delta\lambda^a_s + 2\Delta\lambda^b_s\right) + \alpha\left(p^{trial}_{n+1} - K\alpha\left(\Delta\lambda^a_s + \Delta\lambda^b_s\right)\right) - g_{II}(\phi_{II})\tau_f = 0. \tag{62}$$

With this closed form solution of:

$$\Delta\lambda^a_s = \frac{2G\left(2s^{trial}_{1,n+1} - s^{trial}_{2,n+1} - s^{trial}_{3,n+1} + \alpha p^{trial}_{n+1} - g_{II}(\phi_{II})\tau_f\right) + \alpha^2 K\left(s^{trial}_{1,n+1} - s^{trial}_{2,n+1}\right)}{4G(K\alpha^2 + 3G)}, \tag{63}$$

$$\Delta\lambda^b_s = \frac{2G\left(2s^{trial}_{2,n+1} - s^{trial}_{1,n+1} - s^{trial}_{3,n+1} + \alpha p^{trial}_{n+1} - g_{II}(\phi_{II})\tau_f\right) + \alpha^2 K\left(s^{trial}_{2,n+1} - s^{trial}_{1,n+1}\right)}{4G(K\alpha^2 + 3G)}, \tag{64}$$

$$\Delta\lambda_s = \Delta\lambda^a_s + \Delta\lambda^b_s \tag{65}$$

And the corresponding updates are:

Algorithm 1
Stress Integration

Given: $\boldsymbol{\varepsilon}_n^e, \Delta\boldsymbol{\varepsilon}, \bar{\varepsilon}_n^p, \bar{\varepsilon}_n^s$
Compute trial state for bulk plasticity:
$\boldsymbol{\varepsilon}_{n+1}^{e,trial} = \boldsymbol{\varepsilon}_n^e + \Delta\boldsymbol{\varepsilon}$
$\boldsymbol{\sigma}_{n+1}^{trial} = \dfrac{\partial\psi^e(\boldsymbol{\varepsilon}_{n+1}^{e,trial})}{\partial\boldsymbol{\varepsilon}_{n+1}^{e,trial}}$
$\sigma_{vm,n+1}^{trial} = \sqrt{3J_2(\boldsymbol{\sigma}_{n+1}^{trial})}$
$p_{n+1}^{trial} = \dfrac{I_1(\boldsymbol{\sigma}_{n+1}^{trial})}{3}$
$F_{BP}^{trial} = \sigma_{vm,n+1}^{trial} - \sigma_y(\bar{\varepsilon}_n^p)$
If $F_{BP}^{trial} \geq 0$
Solve (40) for $\Delta\lambda_{BP}$
Update $\boldsymbol{\sigma}_{n+1}$ *and* $\bar{\varepsilon}_{n+1}^p$ with (41), (42)
Else
$\boldsymbol{\sigma}_{bp,n+1} = \boldsymbol{\sigma}_{n+1}^{trial}$
$\bar{\varepsilon}_{n+1}^p = \bar{\varepsilon}_n^p$
Compute trial state for sliding:
$F_s^{trial} = s_{1,n+1}^{trial} - s_{3,n+1}^{trial} + \alpha p_{n+1}^{trial} - g_{II}(\phi_{II})\tau_f$
If $F_s^{trial} \geq 0$
Update $\Delta\lambda_s$ with (45)
Update $s_{1,n+1}, s_{2,n+1}, s_{3,n+1}, p_{n+1}$ *and* $\bar{\varepsilon}_{n+1}^s$ with (46), (47), (48), (49), (50)
If $s_{1,n+1} > s_{2,n+1} > s_{3,n+1}$
Update $\boldsymbol{\sigma}_{n+1}$
$\boldsymbol{\sigma}_{n+1} = \sum_{i=1}^{3}(s_{i,n+1} + p_{n+1})\boldsymbol{e}_i \otimes \boldsymbol{e}_i$
Else
If $s_{1,n+1} + s_{3,n+1} - 2s_{2,n+1} > 0$
Update $\Delta\lambda_s$ with (53), (54), (55)
Update $s_{1,n+1}, s_{2,n+1}, s_{3,n+1}, p_{n+1}$ *and* $\bar{\varepsilon}_{n+1}^s$ with (56), (57), (58), (59) and (60)
Update $\boldsymbol{\sigma}_{n+1}$
$\boldsymbol{\sigma}_{n+1} = \sum_{i=1}^{3}(s_{i,n+1} + p_{n+1})\boldsymbol{e}_i \otimes \boldsymbol{e}_i$
Else
Update $\Delta\lambda_s$ with (63), (64), (65)
Update $s_{1,n+1}, s_{2,n+1}, s_{3,n+1}, p_{n+1}$ *and* $\bar{\varepsilon}_{n+1}^s$ with (66), (67), (68), (69) and (70)
Update $\boldsymbol{\sigma}_{n+1}$
$\boldsymbol{\sigma}_{n+1} = \sum_{i=1}^{3}(s_{i,n+1} + p_{n+1})\boldsymbol{e}_i \otimes \boldsymbol{e}_i$
Else
$\boldsymbol{\sigma}_{n+1} = \boldsymbol{\sigma}_{bp,n+1}$
$\bar{\varepsilon}_{n+1}^s = \bar{\varepsilon}_n^s$

$$s_{1,n+1} = s_{1,n+1}^{trial} - 2G\Delta\lambda_s^a, \tag{66}$$

$$s_{2,n+1} = s_{2,n+1}^{trial} - 2G\Delta\lambda_s^b, \tag{67}$$

$$s_{3,n+1} = s_{3,n+1}^{trial} + 2G\left(\Delta\lambda_s^a + \Delta\lambda_s^b\right), \tag{68}$$

$$p_{n+1} = p_{n+1}^{trial} - \alpha K\left(\Delta\lambda_s^a + \Delta\lambda_s^b\right), \tag{69}$$

$$\bar{\varepsilon}_{n+1}^s = \Delta\lambda_s + \bar{\varepsilon}_n^s. \tag{70}$$

The implemented integration scheme is summarized in Algorithm 1.

Within the COMSOL implementation, the mechanical sub-problem is implemented via the "Solid Mechanics Module" while the mode I and mode II sub-problems are implemented via the "Weak Form PDE Module". In all these modules, the Galerkin finite element discretization is employed. Furthermore, the return mapping equation is implemented in the "Domain ODEs and DAEs Module." The staggered solution scheme from Miehe et al. (2010) was chosen to improve the robustness of the solution scheme. In the implemented staggered scheme, the problems are solved sequentially in the order of the equilibrium equation for ϕ_{II}, the equilibrium equation for ϕ_I and then the equilibrium equation for the displacements. The staggered solver is given 10 iterations in each load increment based on Fei and Choo (2021). Furthermore, a maximum of 0.1 mm of applied displacement is applied in each load increment.

The solution of the nonlinear equilibrium equations for ϕ_I and the displacements were achieved through the standard Newton – Raphson method with a maximum of 20 iterations. If the solver does not converge after taking this many increments, the load increment is cut in half and re-solved.

3. Results and discussion

Before proceeding to 2D examples, each of the models for both fracture modes are tested independently in a 1D setting. The 1D problem consists of a bar with a reduced cross section in the center to force crack nucleation in the center. The geometry and boundary conditions are shown in Fig. 1, along with the model predictions, while arbitrarily chosen material properties are shown in Table 1. For

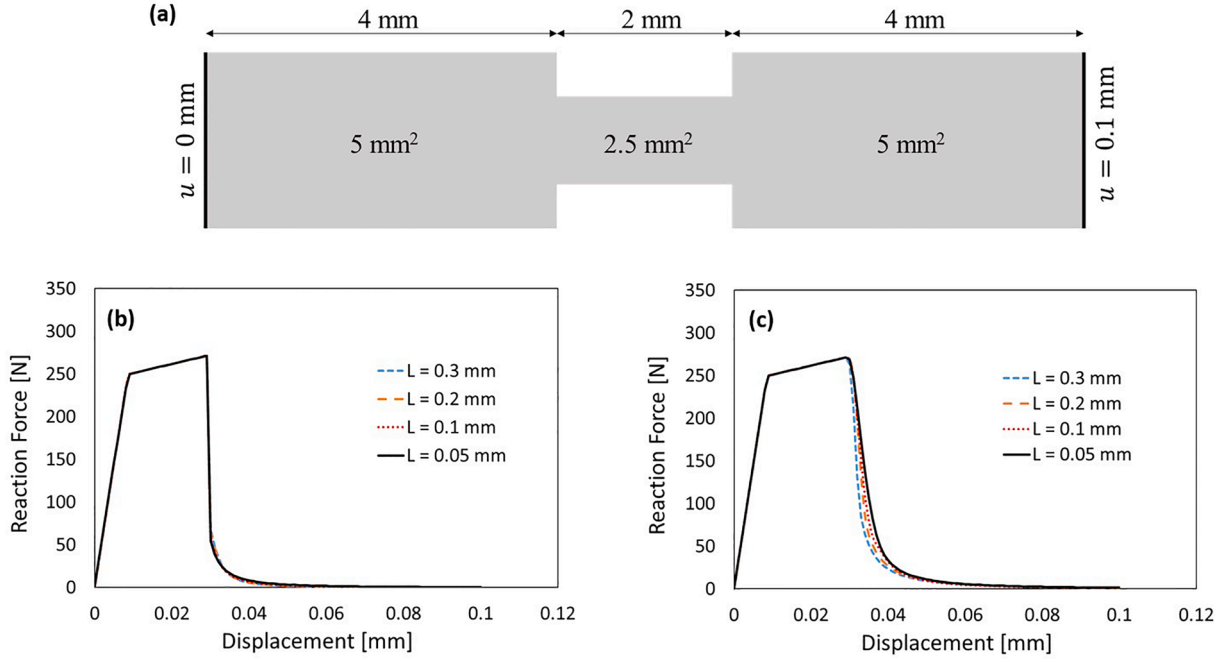

Fig. 1. (a) Geometry and boundary conditions for the 1D problem. (b) Mode I phase field fracture model predictions across multiple regularization length scales. (c) Mode II phase field fracture model predictions across multiple regularization length scales.

Table 1
Material properties for 1D test.

Property	Value
Young's Modulus, E	70 GPa
Plastic Yield Stress, σ_{y0}	100 MPa
Linear Hardening Modulus, H_m	1000 MPa
Critical Mode II Failure Stress, τ_f	110 MPa
Mode I Energetic Damage Threshold, ψ_{cI}^*	0.0864 MPa
Mode I Critical Energy Release Rate, G_{cI}^*	0.5 N/mm
Mode II Critical Energy Release Rate, G_{cII}^*	0.5 N/mm

Table 2
Yield Stress Curve for Al 2024-T351 (Bao, 2003).

Plastic Strain	Yield Stress [MPa]	Plastic Strain	Yield Stress [MPa]
0	320	0.35	660
0.015	380	0.4	680
0.05	460	0.45	700
0.1	510	0.5	720
0.15	550	0.55	730
0.2	580	0.6	740
0.25	610	0.65	743
0.3	640	0.7	745

Table 3
Material properties and Model Parameters for Al 2024-T351.

Property	Value
Young's Modulus, E	70 GPa
Poisson Ratio, ν	0.33
Critical Mode II Failure Stress, τ_f (Bao, 2003)	680 MPa
Mode I Energetic Damage Threshold, ψ^*_{cI}	2.72 MPa
Mode I Critical Energy Release Rate, G^*_{cI} (Mabrouki et al., 2008)	19.8 N/mm
Mode II Critical Energy Release Rate, G^*_{cII} (Mabrouki et al., 2008)	9.8 N/mm
Mode I Degradation Parameter, c	0.3
Pressure Dependence Parameter, α (Xue, 2009)	0.067

the 1D problem, a linear strain hardening behavior is adopted such that the yield stress is given by

$$\sigma_y(\bar{\varepsilon}^p) = \sigma_{y0} + H_m \bar{\varepsilon}^p \tag{71}$$

where σ_{y0} is the initial yield stress and H_m is the linear hardening modulus. Furthermore, a uniform mesh size of 1/5th of the regularization length scale parameter with linear elements is used in these examples as recommended by Carrara et al. (2020), Mandal et al. (2019), Wu and Huang (2020).

From the figure, it is clear that the chosen value of the regularization length scale parameter does not have a significant effect on the mechanical response. This is because the nucleation criteria (Eqs. (22), (23)) of both fracture modes are set independently of the length scale and the fracture energies are convergent with decreasing length scale. Therefore, in the rest of the examples, the regularization length scale parameter is chosen such that it is only a few percent of the geometry's dimension in the loading axis.

Next, the proposed formulation is benchmarked with a set of experiments presented by Bao (2003), Bao and Wierzbicki (2004) and Wierzbicki et al. (2005) on Al 2024-T351. Three experiments which represent a diverse set of triaxiality and lode angles were selected to demonstrate the model's capability in predicting failure under various stress states. Determination of τ_f was completed by equating it to the shear fracture strength based on the provided flow stress curve at the failure equivalent strain from the shear experiment by Bao (2003). On the other hand, ψ^*_{Ic} was determined by probing the maximum value of $\bar{\psi}^e_I$ in an elasto-plastic FE model of the notched round bar specimen when the displacement applied in the simulation is equal to the experimental failure displacement. Values for of G^*_{cI} and G_{cII} were determined from experimental results provided by Mabrouki et al. (2008). The value for α is taken from the work by Xue (2009). Furthermore, the yield stress is supplied to the model in the form of a piecewise linear function determined from the flow stress curves provided in Bao (2003) and has been tabulated in Table 1. The rest of the values used in the numerical examples are summarized in Table 2. For all results, the displacement is measured with the gauge length which was reported as 25.4 mm (Bao, 2003). Further, the mesh size within the region that crack propagation is expected to occur is refined such that the maximum element edge length is 1/5 of the chosen value of the regularization length scale parameter to achieve mesh independent results with fully integrated linear quadrilateral elements as recommended by Carrara et al. (2020), Mandal et al. (2019), Wu and Huang (2020).

3.1. Plane strain tension test

The plane strain tension test is chosen for validation of a high triaxiality, moderate lode angle scenario (Bai and Wierzbicki, 2010). The geometry, boundary conditions and mesh are shown in Fig. 2. Furthermore, regularization length scale parameters of $L_I = 0.3$ mm and $L_{II} = 0.075$ mm were chosen.

Fig. 3 presents the crack path obtained from the simulation. Alongside it, the experimentally obtained crack path from an experiment presented by Teng (2008) is shown. Although the simulation is of the experiment presented in Bao (2003), pictures of a similar plane strain tension experiment for the same material by Teng (2008) better highlight the slant fracture shape (whereas the pictures taken in Bao (2003) were too far away from the specimen for this purpose), which are also captured by the presented model. The prediction of the slant morphology is a product of the information supplied to the model. The ratio of $\frac{\tau_{max}}{\tau_f}$ exceeds that of $\frac{\bar{\psi}^e_I}{\psi^*_{cI}}$ at the onset of failure and causes ϕ_{II} to grow first. Then, the reduction of the mode I strength and toughness due to its coupling with ϕ_{II} causes ϕ_I to grow quickly. When ϕ_I grows rapidly (and causes the opening of the crack faces), the maximum shear strength in the region

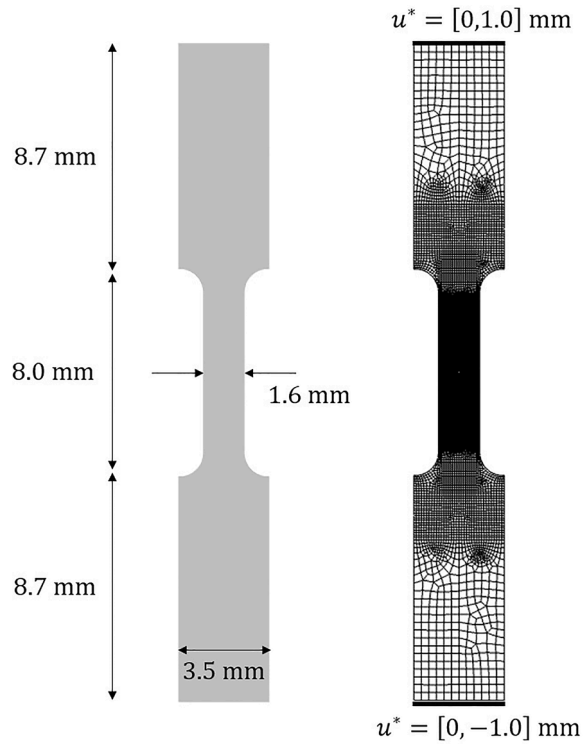

Fig. 2. Geometry, mesh and boundary conditions of the plane strain tension test.

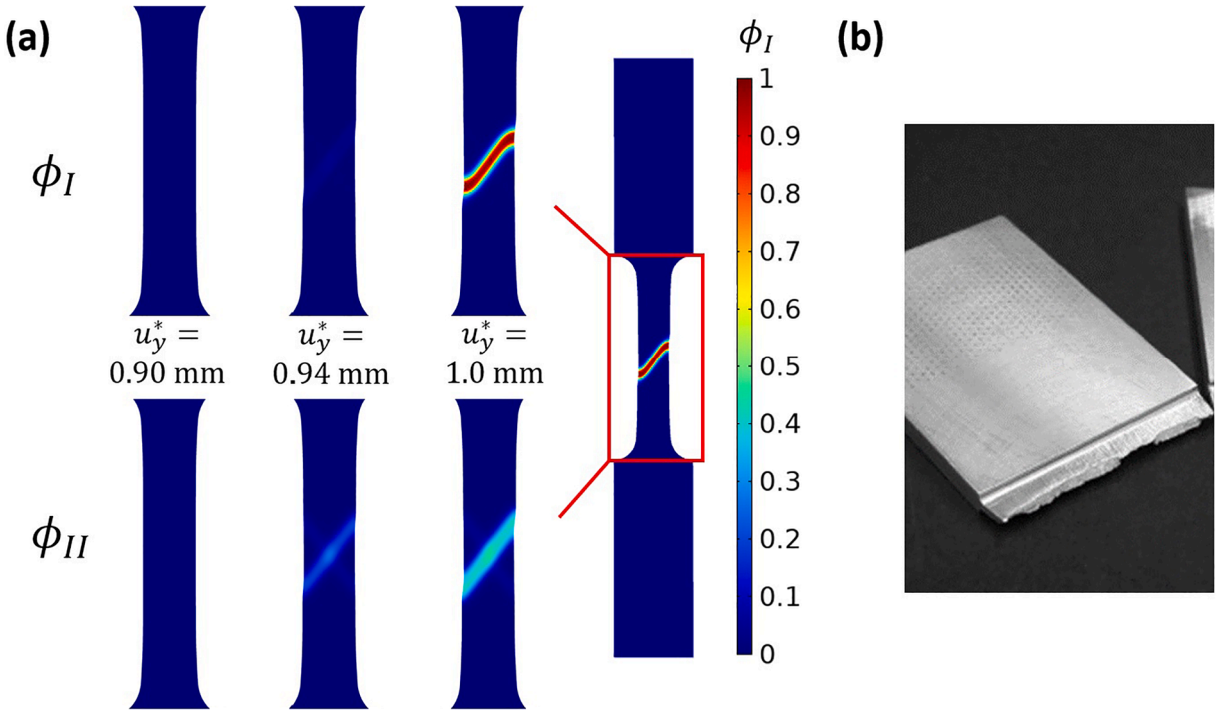

Fig. 3. (a) Crack path evolution of the plane strain tension test, and (b) Comparison to experimentally observed crack path in Teng (2008).

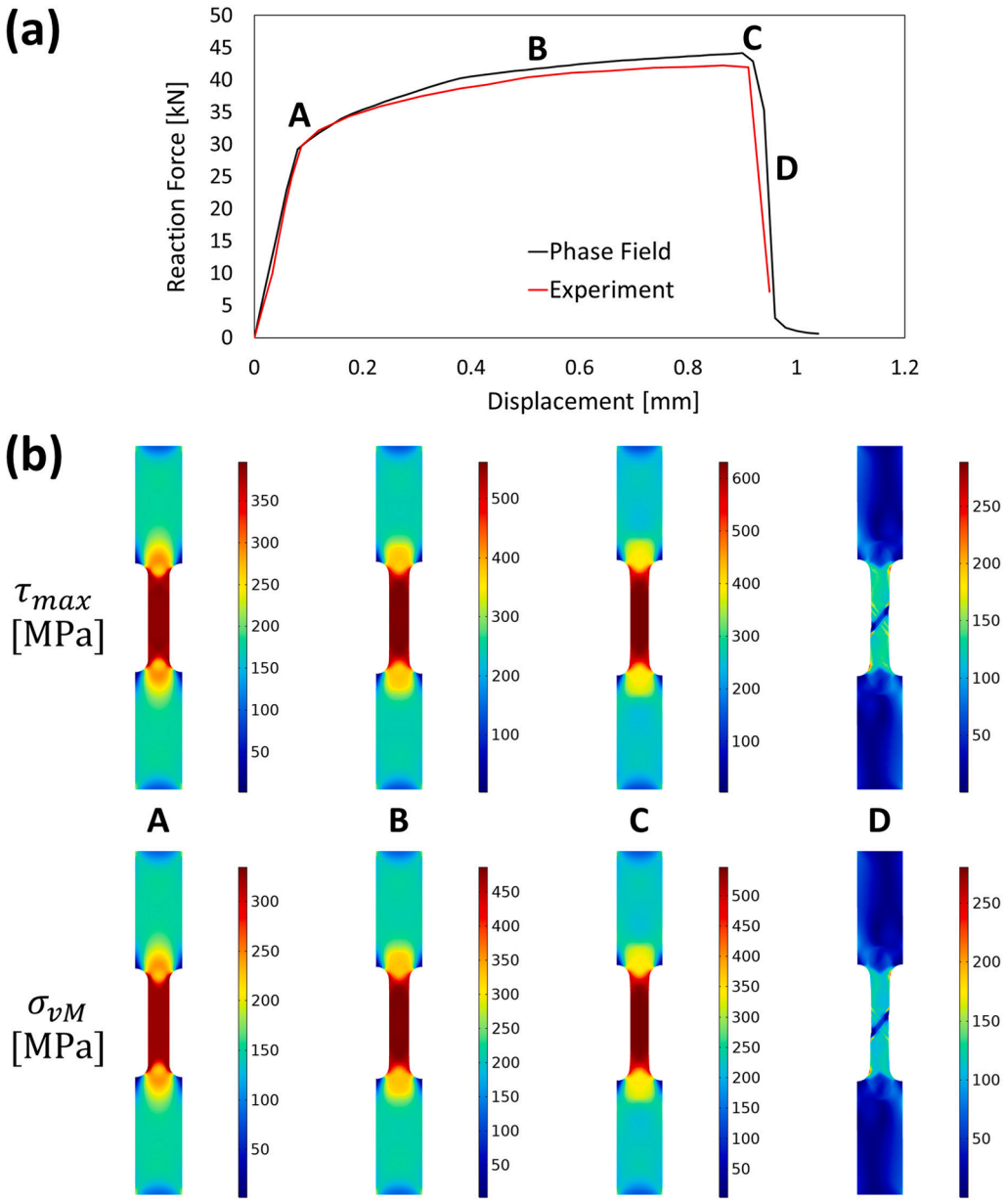

Fig. 4. (a) Predicted and experimental (Bao, 2003) force-displacement curve. (b) Stress contours of the plane strain tension test.

experiencing damage is reduced below the quantity $g_{II}(\phi_{II})\tau_f$ which prevents further growth of ϕ_{II}. Additionally, the flow direction associated with the shear fracture criterion (Eq. (27)) maximizes the deformation along the 45° plane of the geometry. Therefore, accurate predictions of the experimentally observed crack path could be obtained using the proposed model.

Fig. 4 presents a quantitative comparison of the load – displacement curve between the model results and the experiment. The model predicts that the specimen fails when the gauge length deforms 0.90 mm which is very close to the experimentally observed result of 0.91 mm. Additionally, contours of the von Mises stress and maximum shear stress are plotted. From the figures, it can be seen that there is a significant difference between the von Mises and maximum shear stresses. Comparing the initial plastic yield stress from Table 2 with the von Mises stress at point A indicates that plastic yielding for this alloy is mostly dependent on the von Mises stress. On the other hand, comparing τ_f with the maximum shear stress at point C shows that crack nucleation is more dependent on the maximum shear stress. This aspect has been overlooked in many of the previous phase-field models where the effect of the lode angle is not included in the formulation such as in Aldakheel et al. (2018) and Ambati et al. (2016) which can lead to unreliable predictions. In the proposed model, the lode angle implicitly enters into the formulation of a shearing-type fracture since the maximum shear stress can be written in terms of stress invariants as shown in Nayak and Zienkiewicz (1972):

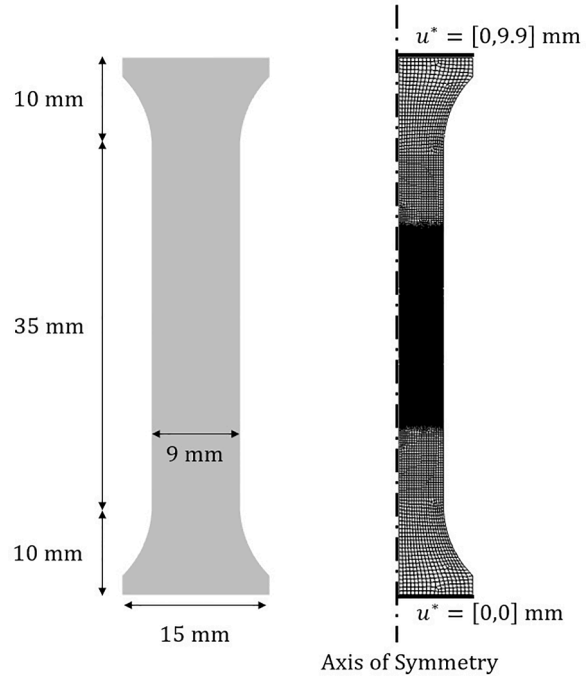

Fig. 5. Geometry, mesh and boundary conditions of the smooth round bar tension test.

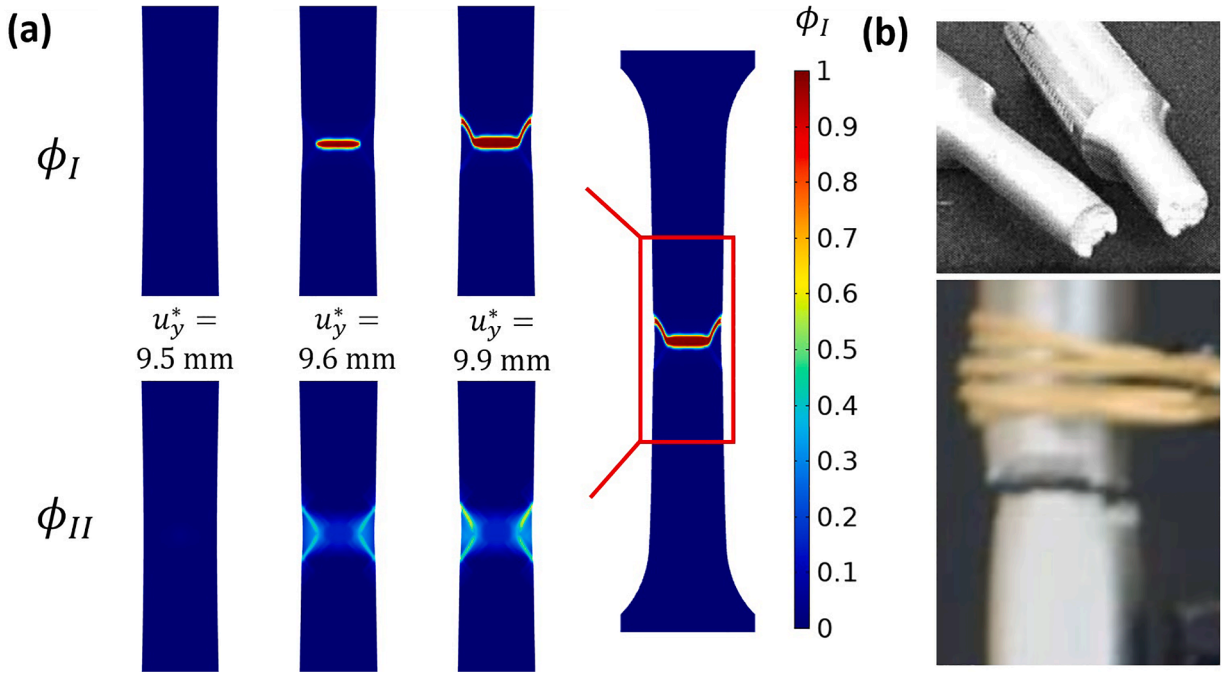

Fig. 6. (a) Crack path evolution of the smooth round bar tension test, and (b) Comparison to the experimentally observed crack path presented in Bao and Wierzbicki (2004), Wierzbicki et al. (2005).

$$\tau_{max} = 2\sqrt{J_2}\cos\left(\theta - \frac{\pi}{6}\right) \tag{72}$$

where θ is the lode angle. The lode angle represents the angle between a given stress state and the projection of the nearest principal stress axis onto the deviatoric plane (Bai et al., 2009). Although a strict interpretation of the lode angle's effect on fracture in alloys has not yet been established, researchers in the past have been able to relate it to a micro-void shearing mechanism (Xue, 2008).

3.2. Smooth round bar

The smooth round bar test is chosen for the validation of a scenario where the triaxiality is moderate and the lode angle is low (Bai and Wierzbicki, 2010). The geometry, boundary conditions and mesh are shown in Fig. 5 and the problem is considered to be axisymmetric. Furthermore, a regularization length scale parameter of $L_I = 0.4$ mm and $L_{II} = 0.1$ mm were chosen.

Fig. 6 depicts the crack path obtained from the simulation. The results clearly show the classic cup-cone shaped crack path. The fracture nucleates from the center of the specimen and propagates normal to the direction of applied load until reaching the surface of the specimen where it propagates in a slanted manner. This occurs because the center of the specimen is subjected to high principal stress (relative to maximum shear stress) which causes the dominance of the mode I fracture in the center of the specimen while the surface of the specimen is subjected to high maximum shear stress which promotes the growth of ϕ_{II} and thus the slant fracture. The crack path is compared to the experimentally obtained fracture surface from Bao (2003) which is shown alongside the simulated crack path to demonstrate the qualitative capability of the model.

Fig. 7 presents a comparison between the experimental load – displacement response and the simulated one. The agreement between the simulated and experimental mechanical response is not as good as in the plane strain scenario but is quite close nonetheless. Further, contours of von Mises stress and maximum shear stress are plotted to illustrate their equivalence in the case of uniaxial tension. This demonstrates that when the effect of the lode angle is neglected from the formulation, an accurate simulation can be performed for the uniaxial tension scenario. However, such accuracy could be misleading as Fig. 4 illustrated.

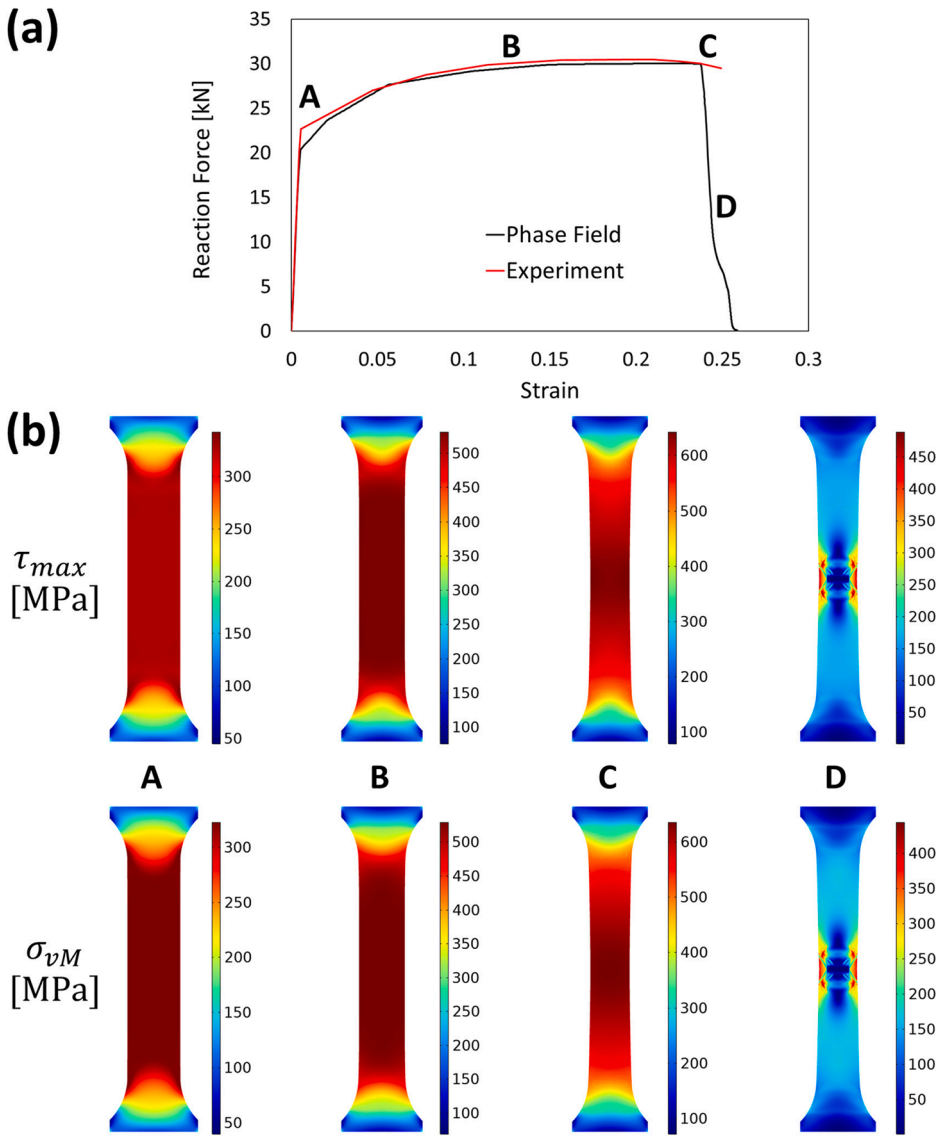

Fig. 7. (a) Predicted and experimental (Bao, 2003) engineering stress strain curve. (b) Stress contours of the smooth round bar tension test.

3.3. Notched round bar

The notched round bar test is chosen for the validation of a scenario where the triaxiality is high and the lode angle is low (Bai and Wierzbicki, 2010). The geometry, boundary conditions and mesh are shown in Fig. 8 and the problem is considered to be

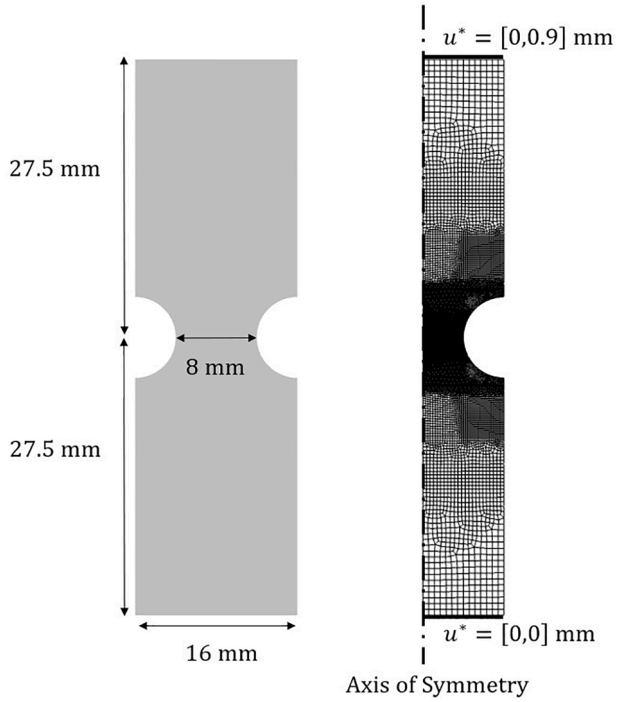

Fig. 8. Geometry, mesh and boundary conditions of the notched round bar tension test.

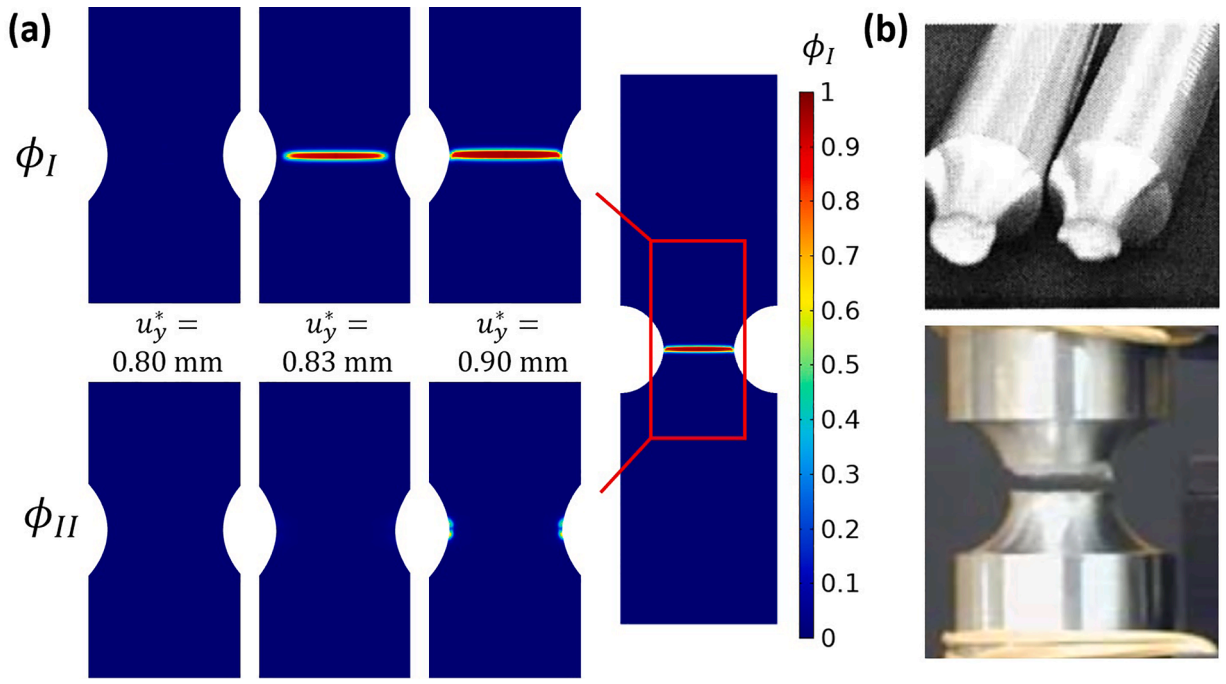

Fig. 9. (a) Crack path evolution of the notched round bar tension test (b) Comparison to the experimentally observed crack path presented in Bao and Wierzbicki (2004), Wierzbicki et al. (2005).

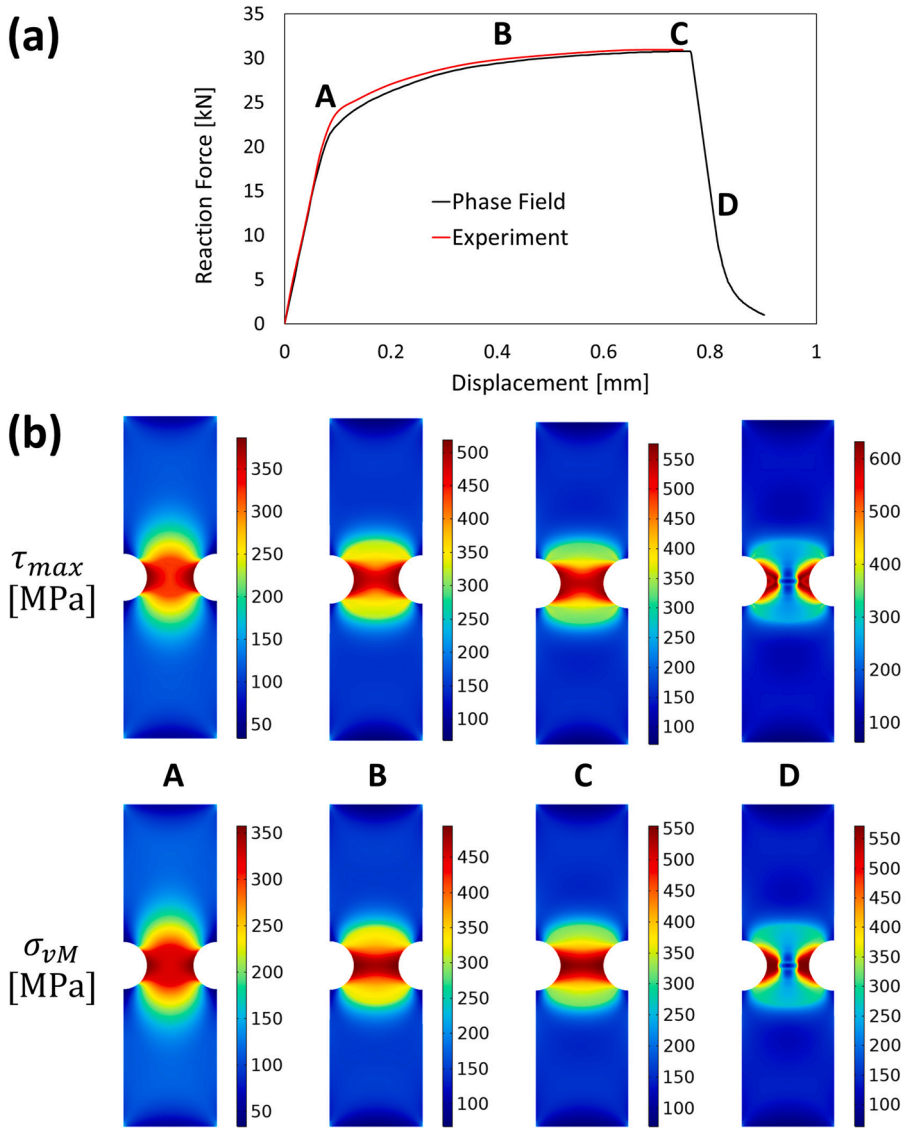

Fig. 10. (a) Predicted and experimental (Bao, 2003) force-displacement curve, and (b) Stress contours of the notched round bar tension test.

axisymmetric. Furthermore, regularization length scale parameters of $L_I = 0.4$ mm and $L_{II} = 0.1$ mm were chosen.

Fig. 9 depicts the crack path obtained from the simulation. The results show a crack path which is completely normal to the applied loading. Contrasted with the case of the smooth round bar, the notch induces a higher triaxial stress state. The higher triaxiality causes the principal stress to be very high relative to the maximum shear stress. This causes ϕ_I to grow rapidly and promote a flat fracture surface. Further, the crack path is compared to the experimentally obtained fracture surface from Bao (2003) which is shown alongside the simulated crack path to demonstrate the qualitative capability of the model. As in the experiment, the crack path is dominated by a flat morphology. A small shear lip is predicted by the simulation at the outer edge of the sample which is consistent with the experiment.

Fig. 10 presents a comparison between the experimental load – displacement response and the simulated one. The simulation results and the experimental results show very close agreement. Further, the maximum shear stress and the von Mises stress are similar before the crack propagates. However, the maximum shear stress quickly becomes significantly higher than the von Mises stress after the crack begins to propagate. The higher maximum shear stress is responsible for the small shear lip.

4. Conclusions

A two-phase field mixed mode framework for modeling of ductile fracture was presented. The presented approach separates opening (ϕ_I) and shearing (ϕ_{II}) type deformations in ductile materials and assigns a crack density functional for each field. As a

consequence of splitting the two responses and the formulation of constitutive relations related to the two phase fields, accurate predictions of the crack path and mechanical response were made. The model predictions were validated with experiments on Al 2024-T351 for different loading scenarios to test the model over a range of stress states.

Depending on the loading scenario, the model was able to reproduce the experimentally observed plane strain slant fracture and cup-cone morphology. Additionally, the model was able to correctly predict the dominantly flat fracture in a sharply notched round bar. Furthermore, unlike many previous phase-field models, the proposed model implicitly includes the effect of the lode angle (via the maximum shear stress) and triaxiality (via the first principal stress and pressure) on the initiation and propagation of ductile fracture which are critical parameters in the ductile fracture process.

CRediT authorship contribution statement

William Huber: Conceptualization, Methodology, Software, Formal analysis, Writing – original draft. **Mohsen Asle Zaeem:** Supervision, Conceptualization, Methodology, Formal analysis, Writing – review & editing, Funding acquisition.

Declaration of Competing Interest

The authors declare that they have no known competing financial interests or personal relationships that could have appeared to influence the work reported in this paper.

Data availability

Data will be made available on request.

Acknowledgment

The authors are grateful for the computer time allocation provided by the Extreme Science and Engineering Discovery Environment (XSEDE) to complete the simulations.

References

Aldakheel, F., Wriggers, P., Miehe, C., 2018. A modified Gurson-type plasticity model at finite strains: formulation, numerical analysis and phase-field coupling. Comput. Mech. 62 (4), 815–833.
Ambati, M., Gerasimov, T., De Lorenzis, L., 2015. Phase-field modeling of ductile fracture. Comput. Mech. 55 (5), 1017–1040. https://doi.org/10.1007/s00466-015-1151-4.
Ambati, M., Kruse, R., De Lorenzis, L., 2016. A phase-field model for ductile fracture at finite strains and its experimental verification. Comput. Mech. 57 (1), 149–167.
Andrade, F., Feucht, M., Haufe, A., Neukamm, F., 2016. An incremental stress state dependent damage model for ductile failure prediction. Int. J. Fract. 200 (1), 127–150.
Bai, Y., Teng, X., Wierzbicki, T., 2009. On the application of stress triaxiality formula for plane strain fracture testing. J. Eng. Mater. Technol. 131 (2).
Bai, Y., Wierzbicki, T., 2010. Application of extended Mohr–Coulomb criterion to ductile fracture. Int. J. Fract. 161 (1), 1–20.
Bao, Y. (2003). *Prediction of ductile crack formation in uncracked bodies* Massachusetts Institute of Technology].
Bao, Y., Wierzbicki, T., 2004. A comparative study on various ductile crack formation criteria. J. Eng. Mater Technol. 126 (3), 314–324.
Borden, M.J., Hughes, T.J., Landis, C.M., Anvari, A., Lee, I.J., 2016. A phase-field formulation for fracture in ductile materials: Finite deformation balance law derivation, plastic degradation, and stress triaxiality effects. Comput. Methods Appl. Mech. Eng. 312, 130–166.
Bourdin, B., Francfort, G.A., Marigo, J.J., 2000. Numerical experiments in revisited brittle fracture. J. Mech. Phys. Solids 48 (4), 797–826.
Carrara, P., Ambati, M., Alessi, R., De Lorenzis, L., 2020. A framework to model the fatigue behavior of brittle materials based on a variational phase-field approach. Comput. Meth. Appl. Mech. Eng. 361, 112731.
Chaboche, J.L. (1988). Continuum damage mechanics: Part I—General concepts.
Comsol,A. (2018). COMSOL multiphysics reference manual, version 5.3. *COMSOL AB*.
De Borst, R., 2003. Numerical aspects of cohesive-zone models. Eng. Fract. Mech. 70 (14), 1743–1757.
de Borst, R., Remmers, J.J., Needleman, A., 2006. Mesh-independent discrete numerical representations of cohesive-zone models. Eng. Fract. Mech. 73 (2), 160–177.
de Borst, R., Verhoosel, C.V., 2016. Gradient damage vs phase-field approaches for fracture: similarities and differences. Comput. Methods Appl. Mech. Eng. 312, 78–94.
De Lorenzis, L., McBride, A., Reddy, B.D., 2016. Phase-field modelling of fracture in single crystal plasticity. GAMM-Mitteil. 39 (1), 7–34.
de Souza Neto, E.A., Peric, D., Owen, D.R., 2011. Computational Methods for Plasticity: Theory and Applications. John Wiley & Sons.
Donovan, P., 1988. Compressive deformation of amorphous Pd40Ni40P20. Mater Sci. Eng. R Rep. 98, 487–490.
Drucker, D.C., 1953. Limit analysis of two and three dimensional soil mechanics problems. J. Mech. Phys. Solids 1 (4), 217–226.
Duda, F.P., Ciarbonetti, A., Sánchez, P.J., Huespe, A.E., 2015. A phase-field/gradient damage model for brittle fracture in elastic–plastic solids. Int. J. Plast. 65, 269–296.
Fei, F., Choo, J., 2021. Double-phase-field formulation for mixed-mode fracture in rocks. Comput. Methods Appl. Mech. Eng. 376, 113655.
Francfort, G.A., Marigo, J.J., 1998. Revisiting brittle fracture as an energy minimization problem. J. Mech. Phys. Solids 46 (8), 1319–1342.
Geelen, R.J., Liu, Y., Hu, T., Tupek, M.R., Dolbow, J.E., 2019. A phase-field formulation for dynamic cohesive fracture. Comput. Methods Appl. Mech. Eng. 348, 680–711.
Griffith, A.A., 1921. The phenomena of rupture and flow in solids. Philos. Trans. R. Soc. Lond. Ser. A 221 (582–593), 163–198. Containing Papers of a Mathematical or Physical Character.
Gurson, A. L. (1977). Continuum theory of ductile rupture by void nucleation and growth: part I—Yield criteria and flow rules for porous ductile media.
Johnson, G.R., Cook, W.H., 1985. Fracture characteristics of three metals subjected to various strains, strain rates, temperatures and pressures. Eng. Fract. Mech. 21 (1), 31–48.
Krajcinovic, D., Lemaitre, J., 1987. Continuum Damage Mechanics: Theory and Applications. Springer.
Kuhn, C., Noll, T., Müller, R., 2016. On phase field modeling of ductile fracture. GAMM-Mitteilungen 39 (1), 35–54.

Lee, Y., Ghosh, J., 1996. The significance of J3 to the prediction of shear bands. Int. J. Plast. 12 (9), 1179–1197.
Lemaitre, J., 1985. Coupled elasto-plasticity and damage constitutive equations. Comput. Methods Appl. Mech. Eng. 51 (1–3), 31–49.
Li, C., Fang, J., Wu, C., Sun, G., Steven, G., Li, Q., 2022. Phase field fracture in elasto-plastic solids: incorporating phenomenological failure criteria for ductile materials. Comput. Methods Appl. Mech. Eng. 391, 114580.
Liu, F., Borja, R.I., 2009. An extended finite element framework for slow-rate frictional faulting with bulk plasticity and variable friction. Int. J. Numer. Anal. Methods Geomech. 33 (13), 1535–1560.
Lloyd, D., 2003. The scaling of the tensile ductile fracture strain with yield strength in Al alloys. Scr. Mater. 48 (4), 341–344.
Lorentz, E., Godard, V., 2011. Gradient damage models: toward full-scale computations. Comput. Methods Appl. Mech. Eng. 200 (21–22), 1927–1944.
Lotfolahpour, A., Asle Zaeem, M., 2021. Effects of cleavage plane and material strength on fracture of polycrystalline brittle materials: a phase-field modeling study. Comput. Mater. Sci. 197, 110642.
Mabrouki, T., Girardin, F., Asad, M., Rigal, J.F., 2008. Numerical and experimental study of dry cutting for an aeronautic aluminium alloy (A2024-T351). Int. J. Mach. Tools Manuf. 48 (11), 1187–1197.
Mandal, T.K., Nguyen, V.P., Wu, J.Y., 2019. Length scale and mesh bias sensitivity of phase-field models for brittle and cohesive fracture. Eng. Fract. Mech. 217, 106532.
Miehe, C., Aldakheel, F., Raina, A., 2016. Phase field modeling of ductile fracture at finite strains: a variational gradient-extended plasticity-damage theory. Int. J. Plast. 84, 1–32.
Miehe, C., Hofacker, M., Schänzel, L.-M., Aldakheel, F., 2015. Phase field modeling of fracture in multi-physics problems. Part II. Coupled brittle-to-ductile failure criteria and crack propagation in thermo-elastic–plastic solids. Comput. Methods Appl. Mech. Eng. 294, 486–522.
Miehe, C., Hofacker, M., Welschinger, F., 2010. A *phase field model for rate-independent crack propagation: Robust algorithmic implementation based on operator splits*. Comput. Methods Appl. Mech. Eng. 199 (45–48), 2765–2778.
Miehe, C., Kienle, D., Aldakheel, F., Teichtmeister, S., 2016. Phase field modeling of fracture in porous plasticity: a variational gradient-extended Eulerian framework for the macroscopic analysis of ductile failure. Comput. Methods Appl. Mech. Eng. 312, 3–50.
Miehe, C., Schaenzel, L.-M., Ulmer, H., 2015. Phase field modeling of fracture in multi-physics problems. Part I. Balance of crack surface and failure criteria for brittle crack propagation in thermo-elastic solids. Comput. Methods Appl. Mech. Eng. 294, 449–485.
Nayak, G., & Zienkiewicz, O. (1972). Elasto-plastic stress analysis. A generalization for various constitutive relations including strain softening.
Needleman, A., Tvergaard, V., 1994. Mesh effects in the analysis of dynamic ductile crack growth. Eng. Fract. Mech. 47 (1), 75–91.
Peerlings, R.H., de Borst, R., Brekelmans, W., Geers, M.G., 1998. Gradient-enhanced damage modelling of concrete fracture. Mech. Cohes. Frict. Mater. Int. J. Exper. Model. Comput. Mater. Struct. 3 (4), 323–342.
Rousselier, G., 1987. Ductile fracture models and their potential in local approach of fracture. Nucl. Eng. Des. 105 (1), 97–111.
Scheider, I., Brocks, W., 2003. Simulation of cup–cone fracture using the cohesive model. Eng. Fract. Mech. 70 (14), 1943–1961.
Scheider, I., Brocks, W., 2006. Cohesive elements for thin-walled structures. Comput. Mater. Sci. 37 (1-2), 101–109.
Schmitt, R., Kuhn, C., Skorupski, R., Smaga, M., Eifler, D., Müller, R., 2015. A combined phase field approach for martensitic transformations and damage. Arch. Appl. Mech. 85 (9), 1459–1468.
Shanthraj, P., Svendsen, B., Sharma, L., Roters, F., Raabe, D., 2017. Elasto-viscoplastic phase field modelling of anisotropic cleavage fracture. J. Mech. Phys. Solids 99, 19–34.
Simoes, M., Martínez-Pañeda, E., 2021. Phase field modelling of fracture and fatigue in shape memory alloys. Comput. Methods Appl. Mech. Eng. 373, 113504.
Spetz, A., Denzer, R., Tudisco, E., Dahlblom, O., 2021. A modified phase-field fracture model for simulation of mixed mode brittle fractures and compressive cracks in porous rock. Rock Mech. Rock Eng. 54 (10), 5375–5388.
Teng, X., 2008. Numerical prediction of slant fracture with continuum damage mechanics. Eng. Fract. Mech. 75 (8), 2020–2041.
Tvergaard, V., 1981. Influence of voids on shear band instabilities under plane strain conditions. Int. J. Fract. 17 (4), 389–407.
Wierzbicki, T., Bao, Y., Lee, Y.W., Bai, Y., 2005. Calibration and evaluation of seven fracture models. Int. J. Mech. Sci. 47 (4–5), 719–743.
Wu, J.Y., Huang, Y., 2020. Comprehensive implementations of phase-field damage models in Abaqus. Theor. Appl. Fract. Mech. 106, 102440.
Wu, J.-Y., Nguyen, V.P., Nguyen, C.T., Sutula, D., Sinaie, S., Bordas, S.P., 2020. Phase-field modeling of fracture. Adv. Appl. Mech. 53, 1–183.
Xue, L., 2008. Constitutive modeling of void shearing effect in ductile fracture of porous materials. Eng. Fract. Mech. 75 (11), 3343–3366.
Xue, L., 2009. Stress based fracture envelope for damage plastic solids. Eng. Fract. Mech. 76 (3), 419–438.
Xue, L., Wierzbicki, T., 2008. Ductile fracture initiation and propagation modeling using damage plasticity theory. Eng. Fract. Mech. 75 (11), 3276–3293.
Yang, Y., Zheng, H., Shi, Z., Zhang, Q., 2011. Effect of orientation on self-organization of shear bands in 7075 aluminum alloy. Mater Sci. Eng. A Struct. Mater. 528 (6), 2446–2453.
Yin, B., Kaliske, M., 2020a. A ductile phase-field model based on degrading the fracture toughness: theory and implementation at small strain. Comput. Meth. Appl. Mech. Eng. 366, 113068.
Yin, B., Kaliske, M., 2020b. Fracture simulation of viscoelastic polymers by the phase-field method. Comput. Mech. 65 (2), 293–309.